Ultralow-Dissipation Superfluid Micromechanical Resonator

F. Souris, X. Rojas,[*] P. H. Kim, and J. P. Davis[†]

Department of Physics, University of Alberta, Edmonton, Alberta T6G 2E9, Canada
(Received 1 August 2016; revised manuscript received 24 January 2017; published 17 April 2017)

Micro- and nanomechanical resonators with ultralow dissipation have great potential as useful quantum resources. The superfluid micromechanical resonators presented here possess several advantageous characteristics: straightforward thermalization, dissipationless flow, and *in situ* tunability. We identify and quantitatively model the various dissipation mechanisms in two resonators, one fabricated from borosilicate glass and one from single-crystal quartz. As the resonators are cryogenically cooled into the superfluid state, the damping from thermal effects and from the normal-fluid component are strongly suppressed. At our lowest temperatures, damping is limited solely by internal dissipation in the substrate materials, and the resonators reach quality factors of up to 913 000 at 13 mK. By lifting this limitation through substrate-material choice and resonator design, modeling suggests that the resonators could reach quality factors as high as 10^8 at 100 mK, putting this architecture in an ideal position to harness mechanical quantum effects and to facilitate the study of superfluids in confined geometries.

I. INTRODUCTION

Recently, there has been heightened interest in micro- and nanomechanical systems as quantum resources, as opposed to traditional—classical—applications such as force [1], mass [2], or torque [3] sensing. For example, mechanics in the quantum regime have demonstrated coupling to microwave qubits [4], entanglement between phonons and photons [5], and quantum-state transduction [6]. Long phonon lifetimes facilitate such quantum operations; hence, resonators for quantum applications are generally made of low-dissipation materials such as single-crystal Si [7] or stressed superconducting aluminum [8]. Yet, these materials are by no means ideal. For example, two-photon adsorption in silicon is a significant limitation for optomechanics at low temperatures [7,9]. The search for improved materials with ultralow mechanical dissipation is actively under way, with studies of high-tension silicon nitride [10] and diamond [11,12], for example. Such materials should also have ultralow dielectric loss in the telecom or microwave bands to be compatible with cavity optomechanics [13]. Development of alternative materials that meet these stringent requirements is, therefore, a key avenue to enabling further progress in quantum nano-mechanics. Recently, it has been realized that a long-studied material, superfluid ^{4}He, is actually one of the most promising candidates for mechanics in the quantum regime [14–18].

Below a critical temperature ($T_\lambda \simeq 2.17$ K), liquid ^{4}He undergoes a transition into a superfluid state, with macroscopic quantum coherence. This state of matter exhibits exotic properties such as frictionless flow below the so-called critical velocity, as well as extremely low mechanical dissipation at millikelvin temperatures. These properties can be described using the two-fluid model, where the fluid is imagined to be composed of a conventional viscous fluid, the normal component ρ_n, and an inviscid fluid, the superfluid component ρ_s. At temperatures that are low compared to T_λ, where the normal-fluid density vanishes ($\rho_n \to 0$), the mechanical properties of the superfluid are expected to be extraordinary. In recent groundbreaking work, mechanical quality factors reaching up to $Q = 1.4 \times 10^8$ were demonstrated by De Lorenzo and Schwab [14,18] in a superfluid acoustic resonator coupled to a superconducting microwave cavity, demonstrating the great potential of superfluid cavity optomechanics.

While the work of De Lorenzo and Schwab [14,18] is performed on gram-scale quantities of superfluid, applicable to the detection of high-frequency gravitational waves [19], quantum optomechanics experiments require larger zero-point fluctuations for the measurement and control of quantum phenomenon: decreasing the mass of the mechanical system increases its usefulness as a quantum resource. Furthermore, confinement to the nanoscale is enticing for the study of superfluids themselves: enabling tests of finite-size scaling theory [20] and prox-imity effects [21] in superfluid ^{4}He, tests for undiscovered superfluid phases [22,23] and surface Majorana fermions in ^{3}He [24–27], and tests of the dynamical response of Tommonoga-Luttinger liquids [28,29].

Recent superfluid-cavity-optomechanics experiments have found that even the small dielectric constant of liquid helium is sufficient to study acoustic modes in fiber cavities [17] and third sound in superfluid films [16]—with

[*]Present address: Department of Physics, Royal Holloway, University of London, Egham, Surrey TW20 0EX, United Kingdom.
[†]jdavis@ualberta.ca

TABLE I.   Comparison of superfluid mechanical resonators.

Reference	$\Omega_m/2\pi$ (kHz)	Mass (kg)	Volume (m³)	$\Gamma_m/2\pi$ (Hz)
De Lorenzo and Schwab [14,18]	8.1	5.7×10^{-3}	4.0×10^{-5}	0.0006
Harris et al. [16]	482	2×10^{-15}	1.4×10^{-17}	106
Kashkanova et al. [17]	317×10^3	3.8×10^{-13}	2.7×10^{-15}	4500
This work	2.9	1.1×10^{-9}	7.3×10^{-12}	0.003

significantly reduced effective masses compared to Ref. [14]. Yet neither these two experiments nor our previous work [15] achieved the ultralow mechanical dissipation of De Lorenzo and Schwab [14]. Therefore, in reduced geometries, dissipation must be systematically revisited to determine the role of confinement. Here, we show that a microgram effective-mass superfluid Helmholtz resonator, in a slab geometry defined by microfabrication [30,31], can achieve ultralow mechanical dissipation, leading to quality factors of up to $Q = 9 \times 10^5$ at 13 mK. For a 3-kHz Helmholtz mode, this quality factor results in a mechanical dissipation rate of $\Gamma_m/2\pi = 3$ mHz—with 10^6 times less effective mass than De Lorenzo and Schwab [14,18]; see Table I—a phonon lifetime of $\tau = Q/\Omega_m \approx 50$ s, and a thermal coherence time of $\tau_{\text{th}} = \hbar Q/k_B T_{\text{bath}} \approx 530$ μs [13].

Furthermore, we are able to quantitatively model the sources of dissipation in this system and find that, at millikelvin temperatures, dissipation is dominated by two-level systems in the microfabricated substrate material. With this knowledge, it will be possible to engineer improvements that would allow this mechanical resonator—which is straightforward to thermalize to millikelvin temperatures and which conceptually could be coupled to a microwave resonator—to achieve quality factors well above 10^7, and thermal coherence times of tens of milliseconds, putting this architecture in an ideal position to harness mechanical quantum effects.

II. FOURTH-SOUND HELMHOLTZ RESONATOR

The premise of a Helmholtz resonator is that a confined fluid can act as a mass-spring system, with the spring constant given by a combination of the compressibility of the fluid and the containment vessel, and the mass given by the moving fluid in the channel. Helmholtz resonances are commonly experienced as the whistle produced when air is blown across the top of a bottle. Confining superfluid ^{4}He likewise leads to a Helmholtz mode and allows us the flexibility to engineer the mode by altering the geometry [15]. Here, the confinement is dictated by microfabricated borosilicate glass [30,31] or single-crystal quartz, with integrated drive electrodes [15]—see Fig. 1. As we discuss in greater detail below, comparing devices fabricated from two different substrate materials allows us to discern the role of the substrate on the dissipation of the Helmholtz resonator.

In this experiment, a microfabricated basin of area A is etched into the substrate material and subsequently patterned with drive electrodes, which are spaced by a distance $h \approx 900$ nm apart after bonding; see Fig. 1 and Appendix A. The basin is connected to the surrounding helium reservoir by four channels, each having cross-section area a and length l. These dimensions, together with the stiffness of the substrate, k_p, and the relative substrate stiffness, $\Sigma = (k_p/2)/k_h$, fully define the superfluid Helmholtz resonance frequency. When a voltage is applied to the electrodes, the substrate bends inward due to the large electrostatic force. In the presence of superfluid helium, this deformation can be used to drive the fourth-sound Helmholtz mode, with an angular resonance frequency

$$\Omega_m = \sqrt{\left(\frac{4a}{l\rho}\right)\frac{\rho_s}{\rho}\frac{k_p/2}{A^2(1+\Sigma)}} \qquad (1)$$
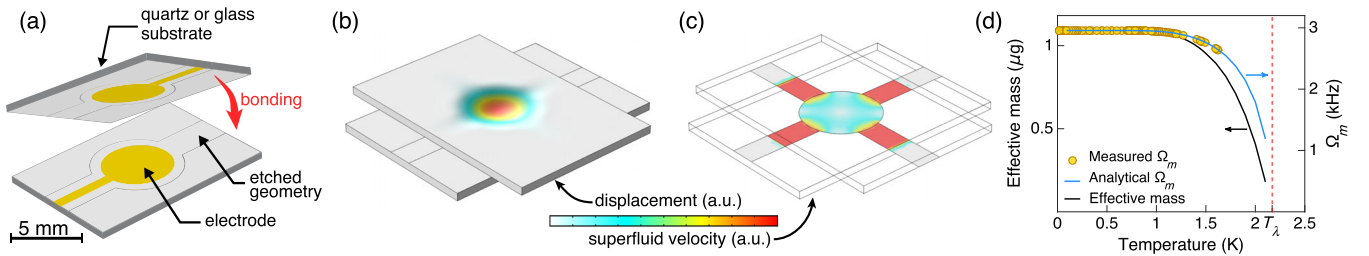

FIG. 1.   Helmholtz-resonator characteristics. (a) Illustration of the resonator microfabrication scheme. The basin and the channels are etched into the substrate (borosilicate glass or single-crystal quartz), chromium and gold electrodes are deposited, and the two substrates are bonded together to create the basin for confining liquid helium. (b) Simulation showing the substrate deflection when a voltage is applied across the two electrodes. The electrostatic force bends the substrate inward, driving the Helmholtz resonance. (c) Simulation of the local superfluid velocity for the Helmholtz resonance. (d) Temperature dependence of the resonance frequency Ω_m measured for the quartz device (the yellow circles), along with the theoretical resonance frequency (the blue curve). The black curve is the corresponding effective mass of the Helmholtz mode, which grows with increasing superfluid density, ρ_s/ρ.

that is proportional to the superfluid density, ρ_s/ρ [15]. That is, the normal-fluid component, ρ_n, is viscously clamped due to the submicron confinement of the channels [see Fig. 1(c) and Appendix D], and the resonance frequency therefore increases as the temperature decreases and the superfluid fraction, ρ_s/ρ, grows [15]. As $T \to 0$, the effective mass of the Helmholtz mode also increases, reaching 1.1 μg, as shown in Fig. 1(d).

III. HIGH-TEMPERATURE DISSIPATION

Unlike the resonance frequency, the temperature dependence of the quality factor, Q, demonstrates complex behavior, as seen in Figs. 2 and 3. For the first device studied here—fabricated from borosilicate glass—the quality factor increases monotonically until approximately 1.2 K and then plateaus. The initial rise in the Q can be understood using the theory derived in Refs. [32,33], which describes the dissipation introduced by the residual motion of the normal fluid in a superfluid Helmholtz resonance. Specifically, when the superfluid oscillates at Ω_m through the channel, the normal fluid is locked to the substrate if the viscous penetration depth, $\lambda = \sqrt{\eta/(\rho_n \Omega_m)}$, is larger than the channel height, $h/2$, with η and ρ_n being the viscosity and the density of the normal fluid, respectively. As discussed in further detail in Appendix D, the normal fluid is not fully clamped to the substrate and its residual motion limits the mechanical quality factor to $Q_n = [(8\eta)/(h/2)^2][\rho_s/(\rho_n^2)][1/(\Omega_m)]$, shown in Fig. 2 as an orange dashed line alongside the experimental data. The model for Q_n results in good agreement with the high-temperature data, considering that no fit parameters are
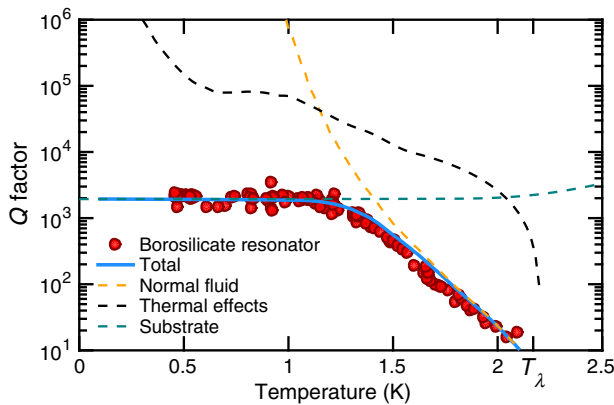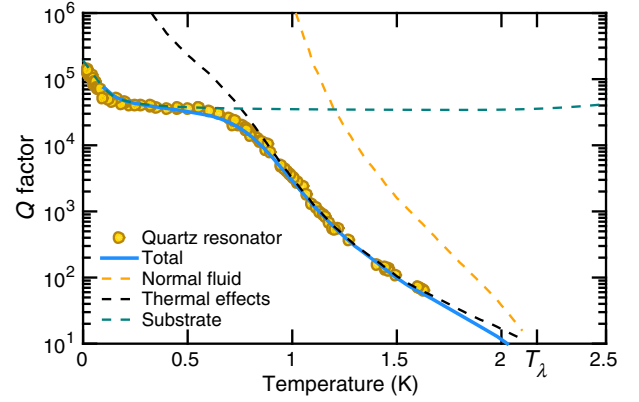

FIG. 3.   An experiment similar to Fig. 2 is reproduced, using a single-crystal quartz substrate instead of borosilicate glass. The quality factor of the quartz resonator (the yellow circles) is measured using a dilution refrigerator from 13 mK to 1.62 K. In contrast to the borosilicate resonator, the damping associated with the normal-fluid residual motion (the dashed orange curve) is now smaller than the one associated with the thermal losses (the dashed black curve). In fact, while keeping the geometry—and hence the normal-fluid damping—nearly constant, the thermal losses are increased because of the high thermal conductivity of crystalline quartz. The green dashed curve is the model of thermally excited two-level systems described in Appendix F. The behavior of the resonator is well reproduced over the entire experimental temperature range.

used. As predicted by the theory, this dissipation mechanism vanishes at low temperature as $\rho_n/\rho \to 0$.

The second device—fabricated from crystalline quartz—also has a high-temperature (700 mK to T_λ) quality factor that monotonically increases as the temperature is reduced; however, its dissipation is dictated by a different physical phenomenon, i.e., thermal losses. As the superfluid moves within the channel, with the normal fluid considered clamped, the amount of superfluid in the basin depletes and replenishes, producing temperature variations, ΔT, due to the mechanocaloric effect [34]. If the basin is perfectly thermally isolated from its environment, we would have $\Delta T = \rho s T \Delta V/c_p$, with s being the specific entropy, c_p the specific heat at constant pressure of the helium in the basin, and ΔV the amount of superfluid displaced. However, the basin walls are not ideal thermal insulators and part of the heat produced leaks out into the superfluid reservoir, providing a thermal bath at the mixing-chamber temperature, T_{mc}, and resulting in mechanical dissipation. This damping mechanism is maximized at high temperature, where ΔT is larger due the large specific entropy, s. Because the crystalline quartz substrate has a significantly larger thermal conductivity [35] and is thinner than the borosilicate-glass substrate, the heat propagates more easily between the basin and the superfluid reservoir, increasing this thermal-loss channel. The model describing the quality factor Q_{th} associated with thermal losses (see Appendix D), shown in Fig. 3 as a dashed black curve, agrees nicely with

FIG. 2.   The quality factor of the borosilicate resonator (the red circles) is measured from 475 mK to 2.09 K using a ^{3}He fridge. The dashed orange curve shows the damping associated with the normal-fluid residual motion and the dashed black curve is a model of thermal losses through the substrate; both are described in Appendix D. Because of the small thermal conductivity of borosilicate, normal-fluid damping is the dominant loss mechanism. The dashed green curve is a prediction of the quality factor expected from internal dissipation in the borosilicate substrate.

the quartz resonator data in the high-temperature region. In this dissipation model, the only parameter adjusted is the area of the basin, A, scaled from the as-fabricated dimensions by a factor of 2. This difference can reasonably be explained by the fact that, as the heat propagates through the substrate of thickness t, the effective area contributing to thermal losses is increased.

IV. LOW-TEMPERATURE DISSIPATION

Remarkably, both thermal losses and the normal-fluid damping model predict exponential growth of the quality factor with lowering temperature that results in the predicted Q's at temperatures below 300 mK exceeding 10^6. On the other hand, our device Q's do not follow this exponential growth at low temperatures, and, moreover, the resonator fabricated from borosilicate glass saturates to about 1800 at 1 K. It is well known that amorphous materials can have a strong acoustic attenuation at audio frequencies and low temperatures due to the presence of two-level systems interacting with the phonons [36,37], which is applicable to borosilicate glass. By measuring a drumlike mechanical resonance mode of an evacuated device (at a significantly higher frequency of $\Omega_{drum} \simeq 220$ kHz), we measure the internal dissipation Q_{drum}^{-1} of the borosilicate material over a broad temperature range of 450 mK to 100 K (see Appendix E). We find that the internal dissipation of the substrate is indeed dominated by the presence of two-level systems, in accordance with other studies [36,37], resulting in $Q_{drum}^{-1} = 7 \times 10^{-4}$. This internal dissipation is found to be frequency independent in the temperature range studied, in agreement with the standard tunneling model [38], and it therefore should be similar for the lower frequency Helmholtz resonance. As discussed in Appendix C, since $1/(1 + \Sigma) = 77\%$ of the potential energy is contained in the substrate stiffness for the borosilicate Helmholtz resonance, two-level system damping accounts for $Q = Q_{drum}/0.77 = 1850$, explaining the saturation of the Q for the glass Helmholtz resonator. A more detailed model for the dissipation arising from two-level systems (see Appendix E) fits well with the low-temperature data of the borosilicate device, as indicated in Fig. 2 by the green dashed curve.

Conveniently, the limitation to the quality factor of an amorphous material can be lifted by employing a substrate material that is ideally exempt of any two-level systems. This possibility motivates us to fabricate the resonator using single-crystal quartz as a substrate since it has been demonstrated to have low acoustic losses at cryogenic temperatures [39,40]. Figure 3 shows that the use of a crystalline substrate substantially reduces the internal dissipation, as the quality factor is now solely limited by the thermal-loss mechanism down to $\simeq 700$ mK, as shown by the good agreement with the theoretical model. If the resonator is cooled down further, however, the quality

factor saturates to a value of $Q = 4 \times 10^4$. To account for this saturation, two extrinsic loss mechanisms are considered first, namely, clamping losses and radiation damping. Clamping loss is a common source of dissipation for mechanical resonators [41], they can become predominant when significant stresses are located near the clamped area of the sample and dissipated into the support structure. This process is unlikely to be responsible for the saturation of the quality factor observed here, as our resonator is loosely attached to the experimental cell through its thin electrical leads. Also, clamping losses are expected to be temperature independent, inconsistent with the subsequent rise of the Q at lower temperature. The second extrinsic loss mechanism considered, radiation damping, happens when a mechanical element dissipates energy by emitting acoustic waves into a surrounding fluid. Applied to our resonator, acoustic emission occurs at the deflected substrate and at the exit of the channels. An analytical and a numerical model, both of which are detailed in Appendix D, show that the energy loss is mitigated by the presence of the copper cell walls, reflecting part of the acoustic energy, as observed in Ref. [42]. As a consequence, we find that radiation damping should limit the quality factor only to a value of approximately 10^8, much higher than the saturation observed.

Instead, we find that this plateau region, and the subsequent rise in the Q at temperatures below 50 mK, can be well described using a model of a two-level system's induced dissipation in the substrate material, unanticipated for single-crystal quartz. The dissipation in the crystalline quartz is modeled as a thermally activated ensemble of two-level systems [43], with an energy splitting of $\Delta E = 1.3$ GHz, described in Appendix F. In this model, the dissipation occurs through an energy transfer between the two-level systems, through the modulation of ΔE by the oscillating elastic strain. As shown in Fig. 3, this simple model describes the changes to the quality factor below 700 mK for the quartz, and, combined with the thermal-dissipation model, the behavior of the resonator can be accurately accounted for over the entire experimental temperature range.

It is interesting to note that, for both the quartz and borosilicate resonators, the quality factor is ultimately limited by internal dissipation in the host material. Hence, reducing the amount of energy stored in the substrate could result in a drastic increase of the Q, up to 10^8 at 100 mK in the case where the dissipation is limited only by thermal losses. Lowering the amount of energy stored in the substrate could be achieved by increasing the substrate stiffness through making the substrate thicker, reducing the diameter of the basin, or patterning pillars that bridge between the two substrates in the area of maximal deflection. Reducing the substrate's internal losses could also lead to an increase of the quality factor, for example, by using diamond substrates that have been shown to have a ΔE of 13 GHz [43]. Likewise, in a subsequent
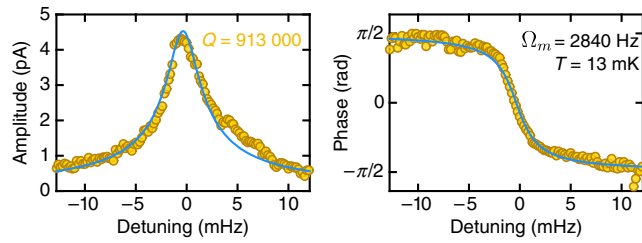
FIG. 4. Superfluid Helmholtz resonance detected at $T = 13$ mK, demonstrating a quality factor of $Q = 913\,000$. For a resonance frequency $\Omega_m = 2840$ Hz, this quality factor results in a phonon lifetime longer than 50 s.

experimental run, after warming up and cooling down the dilution refrigerator with the resonator left untouched in the sample cell, the quality factor of the same quartz Helmholtz is measured to be 913 000 at 13 mK, measured by a ^{60}Co nuclear-orientation thermometer, as shown in Fig. 4. This effect may be attributable to thermal cycling affecting the two-level systems in the substrate and, therefore, the quality factor.

V. SUMMARY

In this work, we fabricate and study the behavior of two superfluid Helmholtz resonators with a submicron confinement. We show that their mechanical dissipation can be accurately modeled from T_λ, where the superfluid resonance takes place, down to $T = 13$ mK, while the mechanical dissipation spans over 4 orders of magnitude. At low temperature, the damping is dominated by the internal dissipation of the substrate materials, and several solutions are offered to mitigate those effects in future experiments. Implementing those solutions could result in quality factors as large as 10^8 at 100 mK, as compared to the 913 000 measured at 13 mK in the present experiment.

Such ultralow-dissipation fluid resonators, with the possibility of engineering confinement, could have numerous applications. For example, they could allow the creation of sensitive detectors to probe small volumes of superfluid ^{3}He, predicted to undergo undiscovered phase transitions in confined geometries [22,23]. Furthermore,

the integration of this mechanical resonator into a microwave cavity, as in Ref. [44], would result in a superfluid optomechanical system with the zero-point fluctuations of the acoustic field, $\Delta P_{\rm zpf} = \sqrt{\hbar \Omega_m / 2 V \chi}$, being enhanced by the small volume of the resonator. Because of the ultralow dielectric loss in the telecom or microwave bands, such a superfluid optomechanical system could potentially be driven to extraordinary cavity-enhanced cooperativities—key to all quantum measurement and control operations [13]. Ultimately, ultralow-dissipation Helmholtz resonances could even be a potential astronomical tool for the detection of a continuous source of gravity waves, as reported by Singh et al. [19].

APPENDIX A: RESONATOR FABRICATION AND GEOMETRY

1. Definition of the geometry

The resonators are built using standard nanofabrication techniques. The geometry is defined by optical lithography, etched into the wafer, and subsequently diced into chips that are bonded together to create the basin and channels of the Helmholtz resonator. The first resonator is fabricated from a 1.1-mm-thick borosilicate wafer, and the second resonator from a 0.5-mm-thick single-crystal Z-cut quartz wafer. In Fig. 5, we define the relevant dimensions of the geometry and show a picture of each resonator. To facilitate comparison, the two resonators are designed to have nearly identical geometries. The two devices differ only by the wafer thickness, t, and the electrode radius, $R_{\rm ele}$, given in Table II, together with other relevant dimensions and properties.
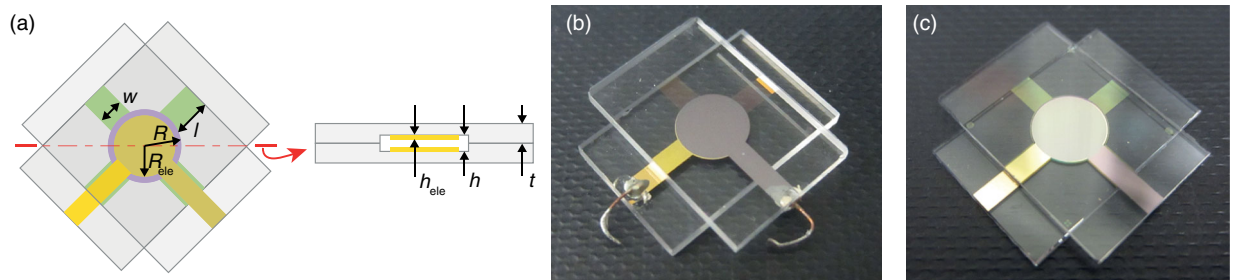

FIG. 5. The Helmholtz resonators are constructed by bonding two microfabricated substrates, forming a central basin and four channels. (a) defines the essential dimensions: the channels are depicted in green, the basin in purple, and the electrodes in yellow. These features are visible in the finished devices, shown in (b) and (c), for the borosilicate and the quartz resonator, respectively.

TABLE II. Summary of the dimensions and physical properties of the two resonators used. The measurement of the substrate spring constant, k_p, is explained in Appendix B.

Parameter	Quartz	Borosilicate
Basin depth h (nm)	1014	1100
Electrodes thickness h_{ele} (nm)	50	100
Basin radius R (mm)	2.5	2.5
Electrode radius R_{ele} (mm)	2.3	2.4
Channel width w (mm)	1.6	1.6
Channel length l (mm)	2.5	2.5
Channel area a (mm^2)	7.3×10^{-4}	7.2×10^{-4}
Basin area A (mm^2)	19.6	19.6
Substrate thickness t (mm)	0.5	1.1
Substrate spring constant k_p (N/m)	1.2×10^7	4.2×10^7

2. Nanofabrication process

The nanofabrication steps used to build the borosilicate and quartz resonators are summarized in Fig. 6. The process starts with a cleaning of the bare quartz (borosilicate) wafer (step A) in a hot piranha solution ($H_2SO_4 + H_2O_2$). After cleaning, a chromium and gold masking layer is sputtered on the wafer (step B). Once developed, the positive photoresist HPR 504, shown in purple in Fig. 6, defines the geometry to be etched onto the wafer (step C). The exposed portion of the masking layer is then removed using chromium and gold etchants (step D), the resist is removed in acetone plus isopropyl alcohol, and the wafer is cleaned in a cold piranha solution. The basin and channels are then etched (step E) with a Borofloat etchant (Silox Vapox III) having an etch rate of 133 nm/min. The masking layer is then removed as in step D and the wafer cleaned again in a hot piranha solution prior to the electrodes' deposition. A chromium and gold layer is deposited that will later create the electrodes. To shape the electrodes, a negative SU-8 photoresist is deposited, exposed, and developed after careful alignment of the mask. The revealed part of the chromium and gold layer is etched away and the photoresist removed with a Remover PG solution. After a dip in a cold piranha bath, the final design is obtained (step F) and the wafer is ready for dicing and bonding. The bonding process is performed under a microscope by manually aligning and pressing two chips together (step G) to obtain the final resonator (step H).

APPENDIX B: DETERMINATION OF THE SUBSTRATE STIFFNESS

When a constant voltage bias, V_{dc}, is applied across the resonator electrodes, the substrate bends under the electrostatic load $q_{ele} = \epsilon_0/2 \times [V_{dc}/(h - h_{ele})]^2$, where ϵ_0 is the vacuum permittivity. Its mean deflection $\bar{x}$, as measured through the capacitance change between the two electrodes, can be used to deduce the substrate spring constant k_p.

The mean deflection of the substrate $\bar{x} = \pi R^2 q_{ele}/k_p$ is obtained by integrating the deflection of a clamped-edge loaded circular plate [45], for which we consider a uniform load distributed over the entire basin area—not applied only to the electrode area—leading to a negligible error in the calculated deflection profile. Since $\bar{x} \ll (h - h_{ele})$, the capacitance C with bent substrates is approximated by $C \simeq C_0 + \gamma V_{dc}^2$. Here, $C_0 = \epsilon_0 \pi R_{ele}^2/(h - h_{ele})$ is the capacitance of the resonator at rest, and

$$\gamma = \left(\frac{C_0}{h - h_{ele}}\right)^2 \left(\frac{R}{R_{ele}}\right)^2 \frac{1}{k_p} \tag{B1}$$

is the capacitance change as a function of V_{dc}^2. The factor $(R/R_{ele})^2$ arises from the fact that the electrode does not cover the entire basin area.

The measurements of C as a function of V_{dc}, presented in Fig. 7, are performed at 4 K and can be safely extrapolated down to millikelvin temperature within 0.1% uncertainty. This extrapolation is safe since the elastic properties of borosilicate and quartz depend very weakly on T in this temperature range [46]. The capacitance shows a linear behavior as a function of V_{dc}^2, as expected for $\bar{x} \ll (h - h_{ele})$. The slope γ, extracted from a linear fit, is used to deduce the substrate spring constant k_p through Eq. (B1). From these measurements, we obtain $k_p = 1.2 \times 10^7$ N/m for the quartz substrate and 4.2×10^7 N/m for the borosilicate, as summarized in Table II.

APPENDIX C: DYNAMICS OF THE SUPERFLUID RESONATOR

1. Mass, stiffness, and resonance frequency of the resonator

A theoretical model describing in detail the reactive and dissipative behavior of a superfluid Helmholtz resonator is derived in Refs. [32,47], including the effects of the normal fluid, thermal expansion, and compressibility. As
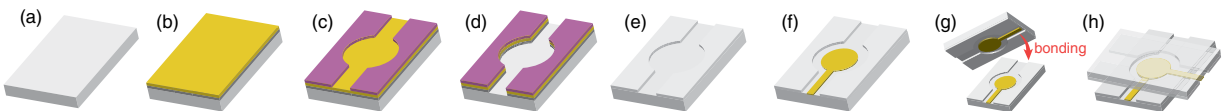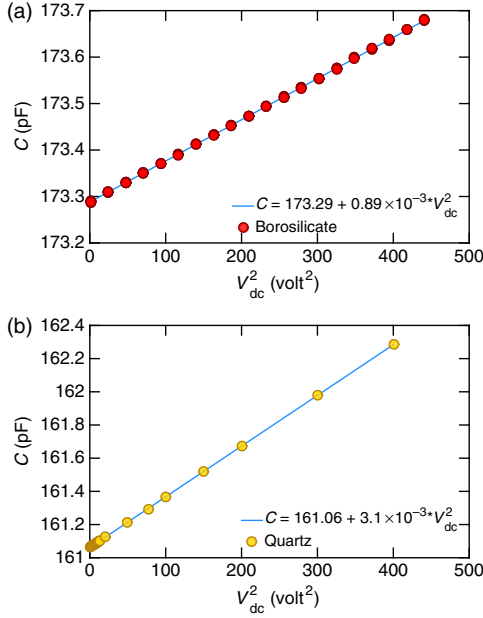

FIG. 6. Various steps of the nanofabrication process, as described in the text. White represents the wafer, yellow the metal masking layer and electrodes, and purple the photoresist.

FIG. 7.   To determine the substrate stiffness, we measure the device capacitance C as a function of the square of the bias voltage: V_{dc}^2. The blue line is a linear fit to the data, from which the slope, γ, is extracted and used to calculate the substrate stiffness, k_p. We find $k_p = 4.2 \times 10^7$ N/m for the borosilicate device and 1.2×10^7 N/m for the quartz.

mentioned by the authors, the final result of those calculations is quite cumbersome. We simplify their result by making few assumptions in application of this model to our resonators. For the current geometry, the main assumptions are that the volume of the superfluid reservoir, V_{res}, surrounding the resonator is large compared to the volume of the basin, i.e., $V \ll V_{res}$, and that we can—at first—neglect dissipative effects to describe the dynamics of the system.

From a simplified point of view, the resonator can be regarded as a mass on a spring system, with the mass being the superfluid moving in the channels (considered as incompressible within the channels) such that $m = 4la\rho_s$. The spring constant, K, with respect to the superfluid displacement, y, arises from a combination in series of the substrate stiffness, K_p, plus the effect of the compressibility of the fluid inside the basin given by K_h. The contribution of the two substrates to the stiffness is given by

$$K_p = \left(\frac{\rho_s}{\rho}\right)^2 \frac{(4a)^2}{A^2} \frac{k_p}{2}, \qquad (C1)$$

where k_p is the substrate stiffness with respect to the mean deflection $\bar{x}$ as defined earlier in Appendix B. In a similar way, we define the contribution of the fluid compressibility

$$K_h = \left(\frac{\rho_s}{\rho}\right)^2 \frac{(4a)^2}{A^2} k_h, \qquad (C2)$$

with $k_h = [A^2/(V\chi)]$ being the stiffness with respect to $\bar{x}$. The resulting stiffness is

$$K = \frac{(4a)^2}{A^2} \left(\frac{\rho_s}{\rho}\right)^2 \frac{k_p/2}{1 + \Sigma}, \qquad (C3)$$

where $\Sigma = (k_p/2)/k_h$ represents the repartitioning of the potential energy between the substrate and the compressed fluid. Therefore, the Helmholtz angular resonance frequency is given by

$$\Omega_m = \sqrt{\frac{K}{m}} = \sqrt{\left(\frac{4a}{l\rho}\right) \frac{\rho_s}{\rho} \frac{k_p/2}{A^2(1 + \Sigma)}}. \qquad (C4)$$

2. Adjustment of the theoretical model to the measured resonance frequency

One particularity of the superfluid Helmholtz resonator, compared to other low-temperature mechanical resonators, is that its resonance frequency Ω_m can be adjusted *in situ* by changing the pressure or the temperature of the superfluid. Indeed, temperature and pressure can strongly affect several thermodynamic functions defining the Helmholtz resonance frequency, such as the superfluid fraction ρ_s/ρ, the density ρ, and the compressibility χ. In the following description, and if not mentioned explicitly in the text, all of the thermodynamic properties for liquid helium are adapted from Ref. [48] and interpolated at the corresponding values of T and P.

To verify how Eq. (C4) applies to a Helmholtz resonator with a slab geometry, with a basin volume much smaller than the one used in previous work [33,49,50], we measure Ω_m for different P, T parameters and adjust Eq. (C4) to this entire data set. More precisely, for each resonator, we perform a temperature scan at a constant P and a pressure scan at a constant T, as shown in Fig. 8. Equation (C4) is fit to our measurements by introducing two parameters, α and β, corresponding to a scaling of Ω_m and a correction to the parameter Σ, respectively, such that

$$\Omega_m = \sqrt{\alpha\left(\frac{4a}{l\rho}\right) \frac{\rho_s}{\rho} \frac{k_p/2}{A^2(1 + \beta\Sigma)}}. \qquad (C5)$$

The fits shown in Fig. 8 have good agreement with the data and Eq. (C5) seems to adequately describe the behavior of Ω_m. For the borosilicate resonator, we obtain $\beta = 2.98$, $\alpha = 2.78$ and, for the quartz, $\beta = 3.4$, $\alpha = 3.1$. It is worth noting that, in both cases, the correction parameters α and β are larger than 1 but are similar between devices. In our geometry, the basin volume is relatively
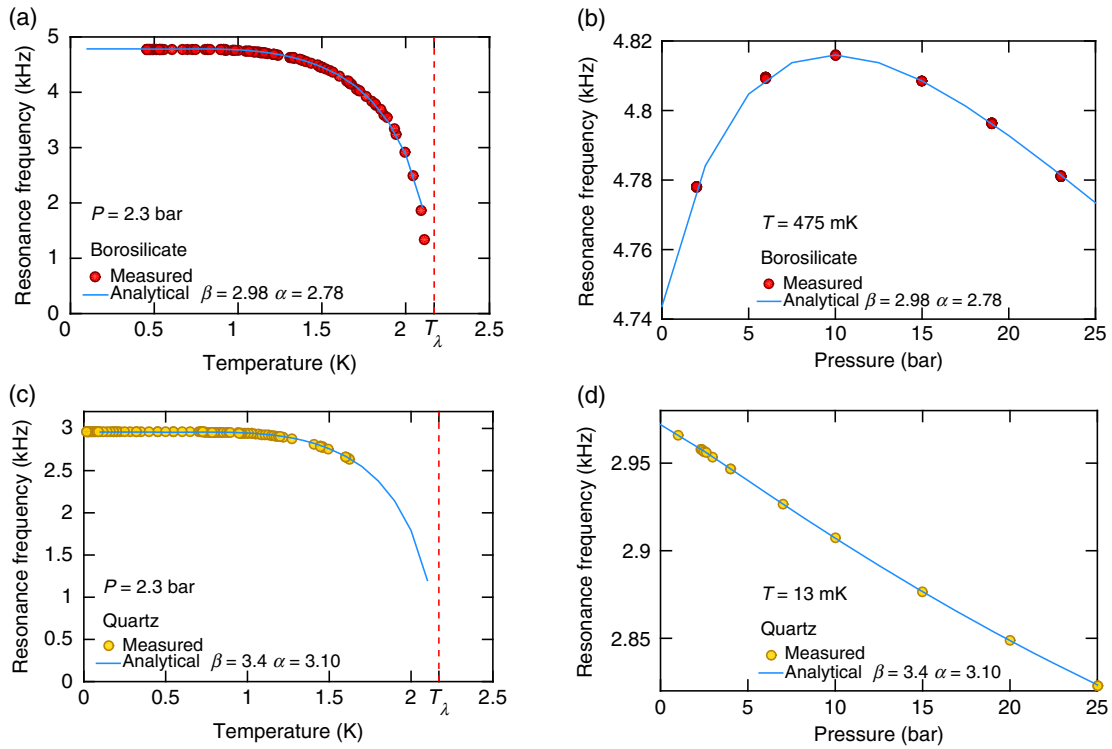
FIG. 8.   For the (a),(b) borosilicate and (c),(d) quartz resonators, the resonance frequency was measured as a function of pressure and temperature. (a) Borosilicate resonator frequency versus temperature with the pressure fixed at $P = 2.3$ bar. (b) Borosilicate resonator frequency versus pressure with the temperature at $T = 475$ mK. (c) Quartz resonator frequency versus temperature with the pressure set at $P = 2.3$ bar. (d) Quartz resonator versus pressure with the temperature set at $T = 13$ mK. The blue curves are fits to Eq. (C5) with two adjustable parameters for each device. Excellent agreement is found for both resonators for a wide pressure and temperature range. For the borosilicate resonator, we find $\beta = 2.98$ and $\alpha = 2.78$ and, for the quartz resonator, $\beta = 3.4$ and $\alpha = 3.1$.

close to the channel volume, and the channel length is of the order of the basin diameter. In this situation, end corrections may be necessary to properly describe the flow. Therefore, these parameters, α and β, account for the discrepancy between our simplistic analytical model and the real system.

The corrected parameter $\beta\Sigma = \beta(k_p/2)/k_h$ gives the ratio of the substrate spring constant to the helium spring constant, which determines the percentage, $1/(1 + \beta\Sigma)$, of potential energy stored in the bending of the substrate. In the case of the quartz resonator, at 2.3 bar, about 91% of the total potential energy is stored in the substrate, compared to 77% for the borosilicate.

APPENDIX D: DISSIPATIVE EFFECTS IN THE SUPERFLUID RESONATOR

1. Normal-fluid dissipation

In Appendix C, the Helmholtz resonance frequency, Ω_m, was derived assuming that the normal component of the fluid is clamped to the substrate and does not contribute to the motion. This condition is fulfilled when the channel height, h_c, is small compared to the viscous penetration depth, $\lambda = \sqrt{\eta/(\rho_n\Omega_m)}$, where η is the viscosity of the

normal fluid. ρ_n and Ω_m depend strongly on temperature, especially near T_λ, and it is not straightforward to *a priori* predict the behavior of the viscous penetration depth in this temperature domain. Therefore, in Fig. 9, we calculate the ratio of the channel height, h_c, to the viscous penetration depth, λ, as a function of T. Below 0.5 K, λ diverges since the normal-fluid fraction vanishes, and it is reasonable to
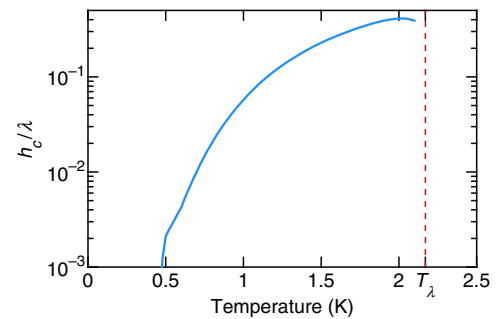

FIG. 9.   When the channel height h_c is small compared to the viscous penetration depth λ, the normal fluid is clamped by its own viscosity. This figure shows the ratio h_c/λ as a function of temperature. Below 0.5 K, $h_c/\lambda \ll 1$, so we can consider that the normal fluid is completely locked.

assume that the normal fluid is fully clamped. However, above 0.5 K, the viscous penetration depth is reduced and, at T_λ, it is only twice that of h_c. Experimentally, as shown above, the behavior of the resonator frequency is well modeled when considering that only the superfluid is moving through the channels, and no corrections from the normal fluid are required. However, the normal fluid not only affects the resonator frequency, it also damps the resonator motion.

When the residual normal-fluid motion and the normal-fluid fraction (ρ_n/ρ) are sufficiently large, viscous damping can become a non-negligible source of dissipation. As mentioned in Ref. [48], in the low-damping limit, the quality factor can be estimated by comparing the average rate of energy dissipation, $\langle D_n \rangle$, due to normal-fluid damping to the total amount of energy stored in the resonator, E, such that $Q_n = E\Omega_m/\langle D_n \rangle$. By applying the theory of Ref. [48] to our resonator geometry, Q_n can be written as

$$Q_n = \frac{8\eta}{(h/2)^2} \frac{\rho_s}{\rho_n^2} \frac{1}{\Omega_m} \left(1 + \frac{\rho_s}{\rho_n} \frac{\alpha_P s T}{c_P} - \frac{\rho_s}{\rho_n} \rho \frac{A^2(1+\Sigma)}{V k_p/2} \frac{s^2 T}{c_P} \right)^{-1},$$
(D1)

with α_P being the isobaric thermal expansion coefficient of liquid helium, c_P the specific heat per unit mass at constant pressure, and s the specific entropy. For our experimental conditions, the last two terms in Eq. (D1) can be neglected and Q_n can be reduced to

$$Q_n = \frac{8\eta}{(h/2)^2} \frac{\rho_s}{\rho_n^2} \frac{1}{\Omega_m}.$$
(D2)

Values for η are extracted from Ref. [51], and values for Ω_m are obtained from the fitting described in Appendix C. Note that the viscous damping is directly proportional to the normal-fluid density and consequently vanishes at low temperatures.

2. Thermal effects in a Helmholtz resonator

When the superfluid oscillates within the channel, the kinetic energy of the superfluid in the channel is converted into potential energy that is stored in the substrate and the superfluid. Ideally, all of the potential energy is released and does not lead to any dissipative effects. However, when the superfluid moves within the channel—with the normal fluid locked to the substrate—it drives a temperature difference, ΔT, between the basin and the helium reservoir due to the resulting imbalance in superfluid ratios: an effect known as the mechanocaloric effect. Because of this temperature difference, heat flows from the basin to the reservoir and is a source of loss. We label Q_{th} the quality factor related to this phenomenon. Calculation of Q_{th} is based on Ref. [32], in which a thorough theoretical analysis

of the response of superfluid Helmholtz resonator is carried out.

The temperature difference, ΔT, has a reactive component in the form of a fountain pressure that acts as an additional spring constant, altering the resonator stiffness and resonance frequency. The importance of this fountain effect compared with the substrate spring constant is evaluated through the parameter

$$\Gamma_{th}^2 = \frac{\rho^2 s^2 T A^2 (1+\Sigma)}{C_{th} k_p/2},$$
(D3)

which is small for our resonator parameters, in that it does not significantly alter Ω_m. The time constant over which this temperature difference returns to equilibrium is given by $\tau_{th} = R_{th} C_{th}$, where R_{th} is the total thermal resistance between the basin and the reservoir and C_{th} is the total heat capacity of the basin. If the driving frequency Ω_m is small compared to $1/\tau_{th}$, the heat loss over a cycle becomes important, leading to energy dissipation. The energy dissipation therefore depends on the parameter $\Phi_{th} = 1/(\Omega_m \tau_{th})$.

A simplified expression for Q_{th} based on Φ_{th} and Γ_{th} can be obtained in two different limits: in the low-temperature limit, the specific entropy is small, leading to $\Gamma_{th}^2 \ll 1$; in the high-temperature limit, entropic effects dominate and we instead use $1 + \Gamma_{th}^2 \gg \Phi_{th}^2$. In those two different limits, Q_{th} is equal to

$$\frac{1+\Phi_{th}^2}{\Phi_{th}\Gamma_{th}^2} \left(1 + \frac{\Gamma_{th}^2}{2(1+\Phi_{th}^2)} \right), \quad \text{if } \Gamma_{th}^2 \ll 1, \quad \text{(D4)}$$

$$\frac{(1+\Gamma_{th}^2)^{3/2}}{\Phi_{th}\Gamma_{th}^2} \left[1 - \frac{(\Gamma_{th}^2-2)}{4(1+\Gamma_{th}^2)} \left(\frac{\Phi_{th}^2}{1+\Gamma_{th}^2} \right) \right], \quad \text{if } 1+\Gamma_{th}^2 \gg \Phi_{th}^2.$$
(D5)

As an example, for the quartz resonator, Γ_{th}^2 is, at most, 6% close to T_λ and is less than 1% below 1.5 K. Therefore, the low-temperature approximation holds over the entire range of temperature and is used to describe the thermal losses in our resonator.

The calculation of Q_{th} also requires knowledge of the total thermal resistance R_{th} between the basin of the resonator and the reservoir surrounding it. R_{th} depends on the geometry of the resonator, and the thermal conductivities of the substrate and the liquid helium. Considering the geometry of the resonator, we can identify two paths through which the heat can flow from the basin to the reservoir, as illustrated in Fig. 10.

The first path propagates through the superfluid-substrate interface, with the Kapitza resistance R_k, the bulk substrate, with the thermal resistivity R_b, and the substrate-superfluid interface, again with the Kapitza
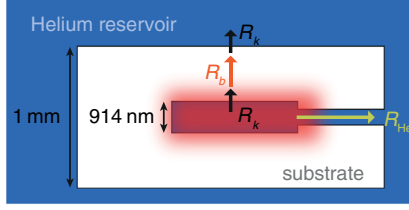
FIG. 10. The oscillation of the superfluid in the channel produces temperature changes inside the basin. The heat can flow in or out the basin by following two main paths, as shown in this sketch of the device. Heat propagation through the substrate requires overcoming two boundary resistances, R_k, and the bulk resistance, R_b. Heat flow through the channels is dictated by the thermal resistance of helium, R_{He}.

resistance R_k. Since those resistances are in series, the total resistance of the first path is given by $R_{th_1} = 2R_k + R_b$.

The second path, illustrated in Fig. 10, propagates through the superfluid in the channel, with the thermal resistivity R_{He}. The total thermal resistance of the second path is, therefore, simply $R_{th_2} = R_{He}$. Since each resonator has, in total, two substrates and four channels, the total thermal resistance is

$$R_{th} = \left(\frac{2}{R_{th_1}} + \frac{4}{R_{th_2}} \right)^{-1}$$

$$= \left(\frac{2}{(2R_k + R_b)} + \frac{4}{R_{He}} \right)^{-1}. \quad (D6)$$

The bulk thermal properties and boundary (Kapitza) resistance for quartz, borosilicate, and helium are summarized in Table III. We took the boundary resistance for borosilicate and helium to be the same as for quartz and helium since it depends primarily on the acoustic impedance mismatch.

For the superfluid in the channel, the thermal conductivity depends on the mean free path Λ of thermal phonons compared to the thickness of the channel h_c. If $\Lambda < h_c$ and the heat flow is small enough to avoid the turbulence of

the superfluid component, the heat flow is laminar and depends on the viscosity η of the normal component. As the temperature is lowered, the mean free path increases and the ballistic regime is reached when Λ becomes comparable to the channel size h_c. In that regime, the thermal conductivity is given by $\kappa = \frac{1}{3} c C_v h_c$ [52,55], where C_v is the specific heat per unit volume and c the phonon velocity. It can be reasonably approximated by $\kappa \simeq 20 h_c T^3$ W/(K cm). In our case, due to the narrow geometry of the channel, the validity of the ballistic regime extends to high temperatures and is used to calculate the thermal conductivity of the superfluid channel across the entire temperature range.

For both the quartz and borosilicate resonators, the thermal resistance through the helium channel is much larger than the resistance through the substrate, and Eq. (D6) can be reduced to $R_{th} = R_k + R_b/2$. In the case of the quartz substrate, since the Kapitza resistance R_k is almost 2 orders of magnitude larger than the thermal resistance of the bulk R_b, Eq. (D6) can be further reduced to $R_{th} = R_k$. By contrast, the Kapitza resistance of borosilicate glass is much smaller than its bulk thermal resistance, and the total thermal resistance can be reduced to $R_{th} = R_b/2$.

3. Radiation damping

a. Analytical model

Because of the finite stiffness k_p of the substrate, pressure oscillations in the basin are associated with a deformation of the walls of the resonator, which in turn can radiate acoustic waves into the surrounding fluid. This energy-loss mechanism, known as radiation damping, depends mostly on the geometry of the resonator and the acoustic impedance of the surrounding fluid, and it is consequently expected to be nearly temperature independent in our case. In order to simplify the model, we first make the assumptions that the surrounding helium is an infinite medium where the sound can propagate freely and that the deformation of the substrate corresponds to the profile of a clamped-edge plate under a uniform load.

TABLE III. Summary of the thermal resistances encountered by the heat flowing from the basin to the surrounding helium reservoir. The thermal conductivity of helium in small channels depends linearly on the channel diameter [52] since it is limited by the mean free path of phonons. Here, we use h_c as the channel diameter.

	Quantity	Units	Quartz[a]	Borosilicate[b]	Helium[c]
Kapitza resistivity with ^{4}He	r_k	(cm^2 K)/W^{-1}	$17.5T^{-3.6}$	$17.5T^{-3.6}$	$\cdots$
Kapitza resistance with ^{4}He	R_k	K W^{-1}	$89.1T^{-3.6}$	$89.1T^{-3.6}$	$\cdots$
Bulk thermal conductivity	κ	W/(cm^{-1} K^{-1})	$0.12T^{2.7}$	$0.25 \times 10^{-3}T^{1.91}$	$20h_cT^3$
Bulk thermal resistance	R_b	K W^{-1}	$2.39T^{-2.7}$	$2.05 \times 10^3 T^{-1.91}$	$3.12 \times 10^7 T^{-3}$

[a]The Kapitza resistivity is extracted from Ref. [53] and the bulk thermal conductivity from Ref. [35].
[b]The Kapitza resistivity for borosilicate is taken to be the same as quartz and the bulk thermal conductivity is obtained from Ref. [54].
[c]The thermal conductivity of helium in small channels is extracted from Ref. [52].

The acoustic properties of a nonuniform acoustic radiator are detailed in Ref. [56] for different plate profiles, but we will focus here on the particular case of a clamped-edge plate profile. We consider a velocity profile of the form

$$v(r) = 3\bar{v}_n \left(1 - \frac{r^2}{R^2}\right)^n H(R - r), \quad (D7)$$

where R is the radius of the plate, H is a step function such that $H(x) = \{0; 1/2; 1\}$ for $\{x\langle 0; x = 0; x\rangle 0\}$, and $\bar{v}_n$ is the average velocity defined as

$$\bar{v} = \frac{1}{\pi R^2} \int_0^\infty v(r) 2\pi r dr. \quad (D8)$$

Those two definitions correspond to the velocity profile and the average velocity used to calculate the effective spring constant in Appendix B. The time-averaged acoustic intensity radiated by an element of the piston is the product of the pressure, p, acting on each element by its velocity v, such that $I = 1/2\text{Re}\{pv^*\}$, where the asterisk denotes the complex conjugate. Then the power emitted is the surface integral $\Pi = \int_S I dS$.

The velocity profile $v(r)$ is known, and the pressure $p(r)$ acting on an element of the piston can be obtained by integrating the contribution of all infinitesimal emitting sources constituting the piston. The calculation of the emitted power Π leads to a reasonable solution when the velocity profile is a simple piston motion [57], but, as shown in Ref. [56], the calculation can still be carried out for the case of a clamped-edge radiator with a nonuniform velocity profile. In this case, one would obtain, for the power radiated,

$$\Pi = \frac{1}{2} \text{Re} \left\{ \frac{9}{5} \rho c (\pi R^2) \bar{v}^2 \right.$$
$$\left. \times \left(1 - \frac{5 \times 2^{11}}{(2kR)^9} [F_1(2kR) + iF_2(2kR)]\right) \right\}, \quad (D9)$$

where k is the wave number of the emitted acoustic wave. The two functions F_1 and F_2 are defined by

$$F_1(y) = (y^4 - 91y^2 + 504)J_1(y) + 14y(y^2 - 18)J_0(y)$$
$$- y^5/16 - y^7/768, \quad (D10)$$

$$F_2(y) = -(y^4 - 91y^2 + 504)H_1(y) - 14y(y^2 - 18)H_0(y)$$
$$+ y^4(14/15\pi) - y^2(168/\pi), \quad (D11)$$

in which J_i is the Bessel function of the first kind of order i and H_j is the Struve function of order j. Equation (D9) can be simplified in the long-wavelength limit, $2kR \ll 1$, where it can be reduced to lowest order in kR to

$$\Pi = \frac{1}{2} \text{Re} \left\{ \rho c (\pi R^2) \bar{v}^2 \right.$$
$$\left. \times \left(\frac{(kR)^2}{2} + i \frac{2^{16}}{3^2 \times 5^2 \times 7 \times 11\pi} (kR)\right) \right\}. \quad (D12)$$

By applying the real operator and rewriting $\bar{v}$ in terms of the mean displacement $\bar{x}$ and resonance frequency Ω_m, we obtain

$$\Pi = \frac{\pi}{4} \frac{\rho}{c} R^4 \Omega_m^4 \bar{x}^2. \quad (D13)$$

It should be noted that, in the low-frequency limit, this result is strictly identical to the result found in the case of a piston with a uniform velocity profile. Although this similarity might seem surprising at first, it can be understood by the fact that, when the radiator's dimensions are small compared to the acoustic wavelength ($2kR \ll 1$), the features of the clamped-edge profile are averaged and only the mean displacement $\bar{x}$ matters.

Now that we can estimate the power radiated by a clamped-edge plate, we can derive the quality factor Q_r associated with those radiation losses for our resonator. In the low-damping limit, it can be estimated by comparing the average power radiated (in our case, 2Π since we have two bending substrates radiating) to the total amount of energy stored in the resonator E. To simplify, we write the total amount of energy E in terms of the mean plate displacement $\bar{x}$ as

$$E = \alpha \frac{k_p}{4} (1 + \beta\Sigma)\bar{x}^2. \quad (D14)$$

The quality factor associated with radiation losses is then

$$Q_r = \Omega_m \frac{E}{2\Pi}$$
$$= \frac{1}{\Omega_m^3} \frac{ck_p \alpha(1 + \beta\Sigma)}{2\pi\rho R^4}. \quad (D15)$$

If we use the parameters and properties defined above for the quartz resonator, and the value of Ω_m in the low-temperature limit, we get $Q_r \simeq 42\,000$.

However, before using this result to our interpret our data, it is important to keep in mind the assumptions made to produce this model. The main assumption consists of assuming that the sound is radiated into an infinite medium. This assumption is, of course, necessary since without it, one would have to deal with the much more complicated problem of reflected sound waves on the different boundaries. Experimentally, however, the resonator is placed inside a closed copper cylindrical cell with a radius $R_{\text{cell}} \simeq$ 10 mm and a height $H_{\text{cell}} \simeq 40$ mm. Therefore, when the sound radiated into the surrounding fluid by the resonator reaches a boundary, it is mainly reflected and partially

transmitted according to the very large acoustic impedance mismatch between liquid helium and copper. In Ref. [42], the effect of reflective boundaries is estimated by multiplying the radiated power by a transmission coefficient $T = (\pi/4)T_0\theta_c$. $T_0 = 4Z_1Z_2/(Z_1 + Z_2)^2$ is the transmission coefficient for an acoustic wave with normal incidence, and $\theta_c = \arcsin(c_1/c_2)$ is the critical angle for total internal reflection from material 1 to material 2. Applied to our cell, this correction coefficient amounts to $T = 1.6 \times 10^{-4}$, limiting the radiation damping to $Q_r = 2.6 \times 10^8$. This analysis is valid only when Ω_m does not overlap with any copper cell resonances. Such an overlap would be confined to a very narrow temperature and pressure range due to the narrow linewidth (on the order of millihertz) of our Helmholtz resonances. Furthermore, we see no evidence experimentally of the mode crossing that was observed in Ref. [42]. However, this method is not quite satisfying analytically since it does not take into account effects like multiple reflections of the acoustic wave on the cell walls, nor does it treat the acoustic emission by the resonator channels.

b. Numerical model

Another method for estimating the quality factor Q_r associated with radiation damping is to apply the finite-element-analysis method used in Ref. [14]. In order to understand how the coupling to the container affects their superfluid resonance, De Lorenzo and Schwab use a numerical model to compute the fraction of energy stored in their container and deduce the associated losses. In a similar fashion, we can numerically compute the fraction of energy radiated and stored in the superfluid surrounding our Helmholtz resonator. Figure 11 shows the result of such a numerical simulation with a quartz resonator surrounded by fluid, oscillating at the Helmholtz resonance frequency Ω_m. The deflection of the substrate and the superfluid flow in the channels both lead to an acoustic emission in the
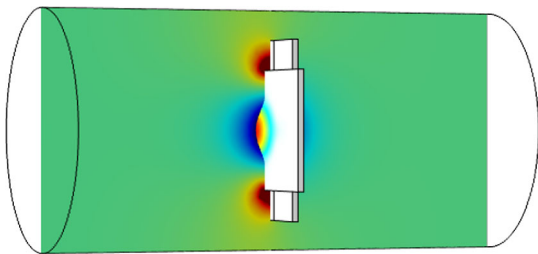

FIG. 11. Numerical simulation of a quartz Helmholtz resonator surrounded by superfluid helium. The color map of the vertical slice represents the acoustic pressure p with arbitrary units. As the substrate bends in and out, it radiates sound into the surrounding fluid, as shown in blue. Associated with the substrate radiation, the moving fluid in the channels also radiates sound out of phase with the substrate, as seen in red.

surrounding fluid, visible as blue and red pressure lobes in Fig. 11.

In order to obtain the potential energy stored in the Helmholtz resonator, we need to add both the elastic potential energy of the bent substrate E_p^{sub} and the potential energy stored in the compressed fluid E_p^{he}, obtained through the quantities

$$E_p^{\text{sub}} = \int \frac{1}{2}\sigma_{ij}\epsilon_{ij}dV, \qquad (D16)$$

$$E_p^{\text{he}} = \int \frac{1}{2}\chi p^2 dV, \qquad (D17)$$

respectively, where σ and ϵ are the stress and strain tensors, respectively, and χ is the compressibility of the superfluid. Using Eq. (D17), the energy stored in the helium inside and surrounding are integrated separately.

First, we can verify that the percentage of energy stored in the substrate agrees with the value of $1/(1 + \beta\Sigma) = 91\%$ measured in Appendix C. The value obtained through the numerical simulation is 86%, showing reasonable quantitative agreement. If we now calculate the percentage of energy stored in the surrounding helium, we find it to be 0.00014%. Since quality factors for helium-filled cavities in copper cells typically lie at around 1000 [58,59], we can estimate $Q_r = 1000/1.4 \times 10^{-6} = 7 \times 10^8$.

In conclusion, we find through two different analyses that radiation damping should only limit the quality factor of the quartz resonator to about 10^8. Additionally, although it is not presented in this article, we detect Helmholtz resonances when only the channels and the basin are filled with superfluid helium, surrounded only by a vacuum. This detection is possible because capillary forces raise the pressure of the fluid in the micron-scale gap and prevent its evaporation. In this situation, the effects of radiation damping are further suppressed.

APPENDIX E: DISSIPATION IN THE BOROSILICATE SUBSTRATE

The quality factor of the Helmholtz resonance for the borosilicate device plateaus at a value of $Q = 1850$ below 1 K. To understand this limitation, we study the behavior of the fundamental drumlike mode of an empty device (Fig. 12). In this situation, the damping arises from internal dissipation in the substrate. The resonance frequency, Ω_{drum}, of this mechanical mode is approximately 220 kHz at the base temperature of our ^{3}He fridge ($T = 475$ mK). Up to $\simeq 5$ K, Ω_{drum} shows a weak temperature dependence, as it changes by less than 0.2%. Above 5 K and up to 100 K, Ω_{drum} decreases by only 2%.

The dissipation of the drumlike resonance, Q_{drum}^{-1}, displays a more complex temperature dependence, yet the behavior of both the Q_{drum}^{-1} and Ω_{drum} can be understood
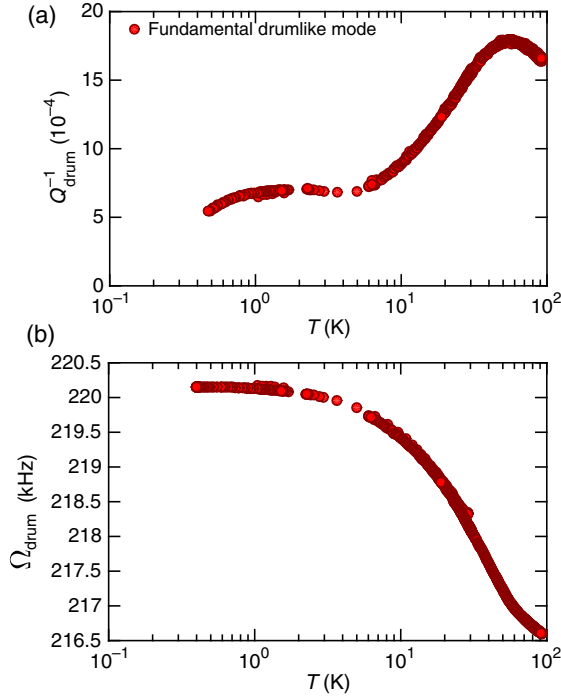
FIG. 12. When the borosilicate device is empty and surrounded by a vacuum, the mechanical resonance of the fundamental drumlike mode is measured as a function of temperature. (a) The dissipation Q_{drum}^{-1} of the drumlike mode as a function of temperature. (b) Resonance frequency Ω_{drum} of the drumlike mode as a function of temperature. As explained in the text, the features of these two curves can be explained by the standard tunneling model of two-level systems [36].

through the standard tunneling model of two-level systems for amorphous materials [36]. Here, the analogy with the measurements of Ref. [36] is striking, as Q_{drum}^{-1} reproduces all of the standard features of such systems. From $T = 475$ mK to 1 K, the dissipation increases with an increasing temperature. Above 1 K and up to 5 K, Q_{drum}^{-1} plateaus at a value of 7×10^{-4}. Finally, a large peak is observed with a maximum value of 18×10^{-4} at 55 K. It is important to note that the drumlike mode has a resonance frequency approximately 50 times higher than the Helmholtz resonance frequency, and the frequency dependence of the dissipation must be considered. The dissipation of two-level systems as a function of frequency has been measured by several groups [38,41] in amorphous SiO_2. The groups' measurements show that, as the frequency is lowered, the temperature of the transition into the plateau region is lowered, down to 100 mK at 5 kHz. The value of the dissipation in the plateau region, however, remains unchanged. Therefore, we expect that, in the temperature range (from 475 mK to T_λ) where the Helmholtz resonance is observed, the internal dissipation of the borosilicate is equal to that in the plateau region, i.e., 7×10^{-4}. In Appendix C, we show that $1/(1 + \Sigma) = 77\%$ of the potential energy is stored in the substrate; therefore, we

predict that the quality factor of the borosilicate Helmholtz resonator should be $Q_{\text{int}} = (1 + \Sigma) \times Q_{\text{drum}} = (0.77 \times 7 \times 10^{-4})^{-1} = 1850$. This result is in good agreement with the value of 1800 ± 300 measured, confirming that the limitation in the quality factor of the resonator is indeed coming from the internal dissipation of the borosilicate.

APPENDIX F: DISSIPATION IN THE QUARTZ SUBSTRATE

1. Two-level systems

The Helmholtz resonance in the borosilicate device is found to be limited by internal dissipation in the substrate material due to two-level systems. Fabricating a Helmholtz resonator from single-crystal Z-cut quartz substantially reduces the losses of the resonator; however, we find that the low-temperature behavior is still dominated by internal dissipation in the substrate. Modeling of the low-temperature dissipation is based on a two-level-system ensemble model, similar to the one used in Ref. [43] to describe dissipation in single-crystal diamond nanoresonators. When the energy splitting of the two-level systems, ΔE, is modulated by the mechanical oscillations, energy is transferred to the two-level systems, with an efficiency depending on the occupation probability of the two-level systems. The quality factor associated with this process, Q_{int}, is given by

$$Q_{\text{int}}^{-1} = \frac{Q_A^{-1}}{(1 + \Sigma)} \frac{e^{-T_0/T}}{e^{T_0/T} + e^{-T_0/T}}. \tag{F1}$$

Here, $T_0 = \Delta E/k_B$, with k_B being the Boltzmann constant. The maximum dissipation in the substrate material Q_A^{-1} is such that $Q_{\text{int}}^{-1}(T \to \infty) = Q_A^{-1}/2$, and $1/(1 + \Sigma)$ is the percentage of potential energy stored in the bending of the substrate, as explained in Appendix C. Applying this model to the low-temperature portion (<500 mK) of the dissipation yields $Q_A = 1.5 \times 10^4$ and $\Delta E = 1.3$ GHz.

2. Drumlike-mode dissipation

A measurement of the drumlike mode, similar to the one performed for the borosilicate device, is made using the quartz resonator, with the results shown in Fig. 13. Owing to the thinner quartz substrate, the resonance frequency is lowered to $\Omega_{\text{drum}} = 155$ kHz. It should be noted that the temperature range covered by this measurement (15 mK to 1 K) is different than the temperature range used in the case of the borosilicate resonator (450 mK to 100 K) due to the cryogenic apparatus used to perform the experiment.

The internal dissipation of the quartz substrate for the drumlike mode measured in Fig. 13(b) plateaus at a value of $Q_{\text{drum}}^{-1} = 7 \times 10^{-7}$, markedly lower than the dissipation measured for the Helmholtz resonance mode in the quartz device at 3 kHz. This result can be explained by the fact that the dissipation associated with two-level systems in
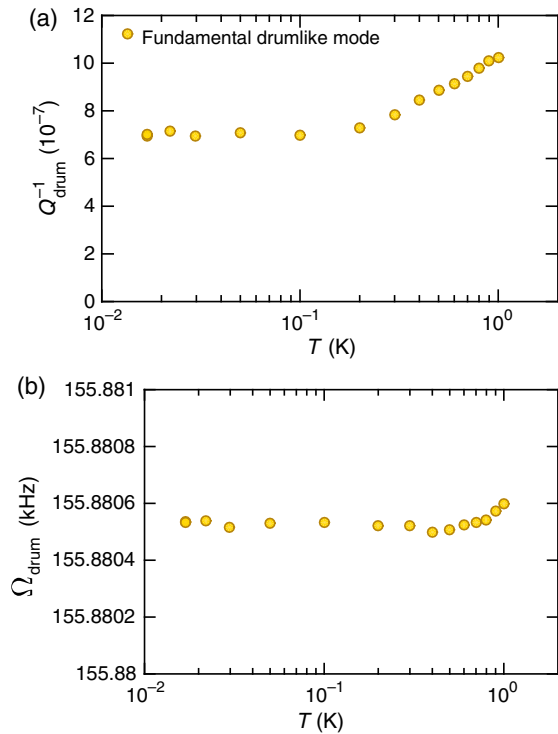
FIG. 13. The mechanical resonance of the fundamental drumlike mode for the quartz resonator. (a) Dissipation of the drumlike mode Q_{drum}^{-1} as a function of temperature. (b) Resonance frequency Ω_{drum} of the drumlike mode as a function of temperature.

crystalline materials depends on the measurement frequency, as has been observed in single-crystal silicon samples [60]. Those measurements showed that, as the frequency is increased, the total dissipation is reduced. Hence, fabricating a resonator with a scaled-down geometry would present a twofold advantage. By increasing the Helmholtz resonance frequency, the internal dissipation of the material would be reduced. Also, the contribution of the substrate to the motion would also be reduced, thereby decreasing the effective damping coming from the material.

[1] H. Miao, K. Srinivasan, and V. Aksyuk, A microelectromechanically controlled cavity optomechanical sensing system, New J. Phys. **14**, 075015 (2012).

[2] J. Chaste, A. Eichler, J. Moser, G. Ceballos, R. Rurali, and A. Bachtold, A nanomechanical mass sensor with yoctogram resolution, Nat. Nanotechnol. **7**, 301 (2012).

[3] P. H. Kim, C. Doolin, B. D. Hauer, A. J. R. MacDonald, M. R. Freeman, P. E. Barclay, and J. P. Davis, Nanoscale torsional optomechanics, Appl. Phys. Lett. **102**, 053102 (2013).

[4] A. D. O'Connell, M. Hofheinz, M. Ansmann, R. C. Bialczak, M. Lenander, E. Lucero, M. Neeley, D. Sank, H. Wang, M. Weides, J. Wenner, J. M. Martinis, and A. N. Cleland, Quantum ground state and single-phonon control of a mechanical resonator, Nature (London) **464**, 697 (2010).

[5] T. A. Palomaki, J. D. Teufel, R. W. Simmonds, and K. W. Lehnert, Entangling mechanical motion with microwave fields, Science **342**, 710 (2013).

[6] F. Lecocq, J. B. Clark, R. W. Simmonds, J. Aumentado, and J. D. Teufel, Mechanically Mediated Microwave Frequency Conversion in the Quantum Regime, Phys. Rev. Lett. **116**, 043601 (2016).

[7] S. M. Meenehan, J. D. Cohen, S. Groblacher, J. T. Hill, A. H. Safavi-Naeini, M. Aspelmeyer, and O. Painter, Silicon optomechanical crystal resonator at millikelvin temperatures, Phys. Rev. A **90**, 011803 (2014).

[8] K. Cicak, D. Li, J. A. Strong, M. S. Allman, F. Altomare, A. J. Sirois, J. D. Whittaker, J. D. Teufel, and R. W. Simmonds, Low-loss superconducting resonant circuits using vacuum-gap-based microwave components, Appl. Phys. Lett. **96**, 093502 (2010).

[9] P. H. Kim, B. D. Hauer, C. Doolin, F. Souris, and J. P. Davis, Approaching the standard quantum limit of mechanical torque sensing, Nat. Commun. **7**, 13165 (2016).

[10] S. S. Verbridge, H. G. Craighead, and J. M. Parpia, A megahertz nanomechanical resonator with room temperature quality factor over a million, Appl. Phys. Lett. **92**, 013112 (2008).

[11] M. Mitchell, B. Khanaliloo, D. P. Lake, T. Masuda, J. P. Hadden, and P. E. Barclay, Single-crystal diamond low-dissipation cavity optomechanics, Optica **3**, 963 (2016).

[12] M. J. Burek, J. D. Cohen, S. M. Meenehan, N. El-Sawah, C. Chia, T. Ruelle, S. Meesala, J. Rochman, H. A. Atikian, M. Markham, D. J. Twitchen, M. D. Lukin, O. Painter, and M. Lončar, Diamond optomechanical crystals, Optica **3**, 1404 (2016).

[13] M. Aspelmeyer, T. J. Kippenberg, and F. Marquardt, Cavity optomechanics, Rev. Mod. Phys. **86**, 1391 (2014).

[14] L. A. De Lorenzo and K. C. Schwab, Superfluid optomechanics: Coupling of a superfluid to a superconducting condensate, New J. Phys. **16**, 113020 (2014).

[15] X. Rojas and J. P. Davis, A superfluid nanomechanical resonator for quantum nanofluidics, Phys. Rev. B **91**, 024503 (2015).

[16] G. I. Harris, D. L. McAuslan, E. Sheridan, Y. Sachkou, C. Baker, and W. P. Bowen, Laser cooling and control of excitations in superfluid helium, Nat. Phys. **12**, 788 (2016).

[17] A. D. Kashkanova, A. B. Shkarin, C. D. Brown, N. E. Flowers-Jacobs, L. Childress, S. W. Hoch, L. Hohmann, K. Ott, J. Reichel, and J. G. E. Harris, Superfluid Brillouin optomechanics, Nat. Phys. **13**, 74 (2017).

[18] L. A. De Lorenzo and K. C. Schwab, Ultra-high Q acoustic resonance in superfluid ^{4}He, J. Low Temp. Phys. **186**, 233 (2017).

[19] S. Singh, L. A. De Lorenzo, I. Pikovski, and K. C. Schwab, Detecting continuous gravitational waves with superfluid ^{4}He, arXiv:1606.04980.

[20] F. M. Gasparini, M. O. Kimball, K. P. Mooney, and M. Diaz-Avila, Finite-size scaling of ^{4}He at the superfluid transition, Rev. Mod. Phys. **80**, 1009 (2008).

[21] J. K. Perron and F. M. Gasparini, Critical Point Coupling and Proximity Effects in ^{4}He at the Superfluid Transition, Phys. Rev. Lett. **109**, 035302 (2012).

[22] A. B. Vorontsov and J. A. Sauls, Crystalline Order in Superfluid ^{3}He Films, Phys. Rev. Lett. **98**, 045301 (2007).

[23] J. J. Wiman and J. A. Sauls, Superfluid phases of ^{3}He in nanoscale channels, Phys. Rev. B **92**, 144515 (2015).

[24] S. B. Chung and S.-C. Zhang, Detecting the Majorana Fermion Surface State of ^{3}He-B through Spin Relaxation, Phys. Rev. Lett. **103**, 235301 (2009).

[25] T. Mizushima, Superfluid ^{3}He in a restricted geometry with a perpendicular magnetic field, Phys. Rev. B **86**, 094518 (2012).

[26] H. Wu and J. A. Sauls, Majorana excitations, spin and mass currents on the surface of topological superfluid ^{3}He-B, Phys. Rev. B **88**, 184506 (2013).

[27] L. V. Levitin, R. G. Bennett, A. Casey, B. Cowan, J. Saunders, D. Drung, Th. Schurig, and J. M. Parpia, Phase diagram of the topological superfluid ^{3}He confined in a nanoscale slab geometry, Science **340**, 841 (2013).

[28] J. Taniguchi, Y. Aoki, and M. Suzuki, Superfluidity of liquid ^{4}He confined to one-dimensional straight nanochannel structures, Phys. Rev. B **82**, 104509 (2010).

[29] J. Taniguchi, K. Demura, and M. Suzuki, Dynamical superfluid response of ^{4}He confined in a nanometer-size channel, Phys. Rev. B **88**, 014502 (2013).

[30] A. Duh, A. Suhel, B. D. Hauer, R. Saeedi, P. H. Kim, T. S. Biswas, and J. P. Davis, Microfluidic and nanofluidic cavities for quantum fluids experiments, J. Low Temp. Phys. **168**, 31 (2012).

[31] X. Rojas, B. D. Hauer, A. J. R. MacDonald, P. Saberi, Y. Yang, and J. P. Davis, Ultrasonic interferometer for first-sound measurements of confined liquid ^{4}He, Phys. Rev. B **89**, 174508 (2014).

[32] S. Backhaus and E. Yu. Backhaus, Thermoviscous effects in steady and oscillating flow of an isotropic superfluid: Theory, J. Low Temp. Phys. **109**, 511 (1997).

[33] J. S. Brooks, B. B. Sabo, P. C. Schubert, and W. Zimmermann, Jr., Helmholtz-resonator measurements of the superfluid density of liquid ^{4}He in submicrometer-diameter channels, Phys. Rev. B **19**, 4524 (1979).

[34] S. W. Van Sciver, *Helium Cryogenics*, 2nd ed. (Springer, New York, 2012), p. 193.

[35] J. W. Gardner and A. C. Anderson, Low-temperature specific heat and thermal conductivity of neutron-irradiated crystalline quartz, Phys. Rev. B **23**, 474 (1981).

[36] J. Classen, C. Enss, C. Bechinger, G. Weiss, and S. Hunklinger, Low frequency acoustic and dielectric measurements on glasses, Ann. Phys. (Berlin) **506**, 315 (1994).

[37] K. A. Topp and D. G. Cahill, Elastic properties of several amorphous solids and disordered crystals below 100 K, Z. Phys. B **101**, 235 (1996).

[38] A. D. Fefferman, R. O. Pohl, A. T. Zehnder, and J. M. Parpia, Acoustic Properties of Amorphous Silica between 1 and 500 mK, Phys. Rev. Lett. **100**, 195501 (2008).

[39] S. Galliou, J. Imbaud, M. Goryachev, R. Bourquin, and P. Abbé, Losses in high quality quartz crystal resonators at cryogenic temperatures, Appl. Phys. Lett. **98**, 091911 (2011).

[40] S. Galliou, M. Goryachev, R. Bourquin, P. Abbé, J.-P. Aubry, and M. E. Tobar, Extremely low loss phonon-trapping cryogenic acoustic cavities for future physical experiments, Sci. Rep. **3**, 2132 (2013).

[41] J. Classen, T. Burkert, C. Enss, and S. Hunklinger, Anomalous Frequency Dependence of the Internal Friction of Vitreous Silica, Phys. Rev. Lett. **84**, 2176 (2000).

[42] D. Schmoranzer, M. La Mantia, G. Sheshin, I. Gritsenko, A. Zadorozhko, M. Rotterand, and L. Skrbek, Acoustic emission by quartz tuning forks and other oscillating structures in cryogenic ^{4}He fluids, J. Low Temp. Phys. **163**, 317 (2011).

[43] Y. Tao, J. M. Boss, B. Moores, and C. L. Degen, Single-crystal diamond nanomechanical resonators with quality factors exceeding one million, Nat. Commun. **5**, 3638 (2014).

[44] M. Yuan, V. Singh, Y. M. Blanter, and G. A. Steele, Large cooperativity and microkelvin cooling with a three-dimensional optomechanical cavity, Nat. Commun. **6**, 8491 (2015).

[45] R. C. Young and R. G. Budynas, *Roark's Formulas for Stress and Strain*, 7th ed. (McGraw-Hill, New York, 1992), p. 488.

[46] A. K. Raychaudhuri and S. Hunklinger, Low frequency elastic properties of glasses at low temperatures—Implications on the tunneling model, Z. Phys. B **57**, 113 (1984).

[47] S. Backhaus, K. Schwab, A. Loshak, S. Pereverzev, N. Bruckner, J. C. Davis, and R. E. Packard, Thermoviscous effects in steady and oscillating flow of superfluid ^{4}He: Experiments, J. Low Temp. Phys. **109**, 527 (1997).

[48] J. S. Brooks and R. J. Donnelly, The calculated thermodynamic properties of superfluid helium-4, J. Phys. Chem. Ref. Data **6**, 51 (1977).

[49] O. Avenel and E. Varoquaux, Observation of Singly Quantized Dissipation Events Obeying the Josephson Frequency Relation in the Critical Flow of Superfluid ^{4}He through an Aperture, Phys. Rev. Lett. **55**, 2704 (1985).

[50] B. P. Beecken and W. Zimmermann, Search for an ac Josephson effect in superfluid ^{4}He using a low-frequency acoustic resonator, Phys. Rev. B **35**, 74 (1987).

[51] R. Donnelly and C. Barenghi, The observed properties of liquid helium at the saturated vapor pressure, J. Phys. Chem. Ref. Data **27**, 1217 (1998).

[52] D. S. Greywall, Thermal-conductivity measurements in liquid ^{4}He below 0.7 K, Phys. Rev. B **23**, 2152 (1981).

[53] G. L. Pollack, Kapitza resistance, Rev. Mod. Phys. **41**, 48 (1969).

[54] F. Pobell, *Matter and Methods at Low Temperatures*, 3rd ed. (Springer, New York, 2007), p. 71.

[55] M. Sciacca and L. Galantucci, Effective thermal conductivity of superfluid helium: Laminar, turbulent and ballistic regimes, Commun. Appl. Ind. Math. **7**, 111 (2016).

[56] M. Greenspan, Piston radiator: Some extensions of the theory, J. Acoust. Soc. Am. **65**, 608 (1979).

[57] P. M. Morse, *Vibration and Sound*, 2nd ed. (McGraw-Hill, New York, 1948), p. 326.

[58] X. Rojas, A. Haziot, V. Bapst, S. Balibar, and H. J. Maris, Anomalous Softening of ^{4}He Crystals, Phys. Rev. Lett. **105**, 145302 (2010).

[59] F. Souris, A. D. Fefferman, A. Haziot, N. Garroum, J. R. Beamish, and S. Balibar, Search for dislocation free helium 4 crystals, J. Low Temp. Phys. **178**, 149 (2015).

[60] R. N. Kleiman, G. Agnolet, and D. J. Bishop, Two-Level Systems Observed in the Mechanical Properties of Single-Crystal Silicon at Low Temperatures, Phys. Rev. Lett. **59**, 2079 (1987).